Nature Communications

https://doi.org/10.1038/s41467-026-72887-7

Article in Press

Chip-integrated metasurface with double-helix point spread functions for ultra-large dynamic range wavefront sensing

Received: 5 December 2025

Accepted: 27 April 2026

Cite this article as: Chu, Y., Li, X., Long, X. *et al.* Chip-integrated metasurface with double-helix point spread functions for ultra-large dynamic range wavefront sensing. *Nat Commun* (2026). https://doi.org/10.1038/s41467-026-72887-7

Yanhao Chu, Xiaopeng Li, Xian Long, Jiacheng Sun, Jian Li, Jitao Ji, Junyi Wang, Shining Zhu & Tao Li

Chip-Integrated Metasurface with Double-Helix Point Spread Functions for Ultra-Large Dynamic Range Wavefront Sensing

Authors

Yanhao Chu[1,2,3,4,†], Xiaopeng Li[1,2,3,4,†], Xian Long[1,2,3,4,*], Jiacheng Sun[1,2,3,4], Jian Li[1,2,3,4], Jitao Ji[1,2,3,4], Junyi Wang[1,2,3,4], Shining Zhu[1,2,3,4] & Tao Li[1,2,3,4,*]

1. National Laboratory of Solid State Microstructures, College of Engineering and Applied Sciences, Nanjing University, Nanjing 210093, China.
2. Key Laboratory of Intelligent Optical Sensing and Manipulations, Nanjing University, Nanjing 210093, China.
3. Jiangsu Key Laboratory of Artificial Functional Materials, Nanjing University, Nanjing 210093, China.
4. Collaborative Innovation Center of Advanced Microstructures, Nanjing University, Nanjing 210093, China.

†These authors contributed equally to this work.

*Correspondence and requests for materials should be addressed to Xian Long, loonggodx@nju.edu.cn, and Tao Li, taoli@nju.edu.cn.

Abstract

Wavefront sensing underpins diverse optical technologies, requiring compact sensors with large dynamic range, high spatial sampling density, and photonic integration. Conventional Shack-Hartmann sensors offer only ~±1° intrinsic geometric dynamic range, ~10 sub-apertures per millimeter, and cannot resolve polarization-dependent wavefronts. Existing metasurface-based approaches still require external imaging optics, preventing true on-chip integration. Critically, both schemes suffer from an inherent trade-off between dynamic range and sampling density. Here,

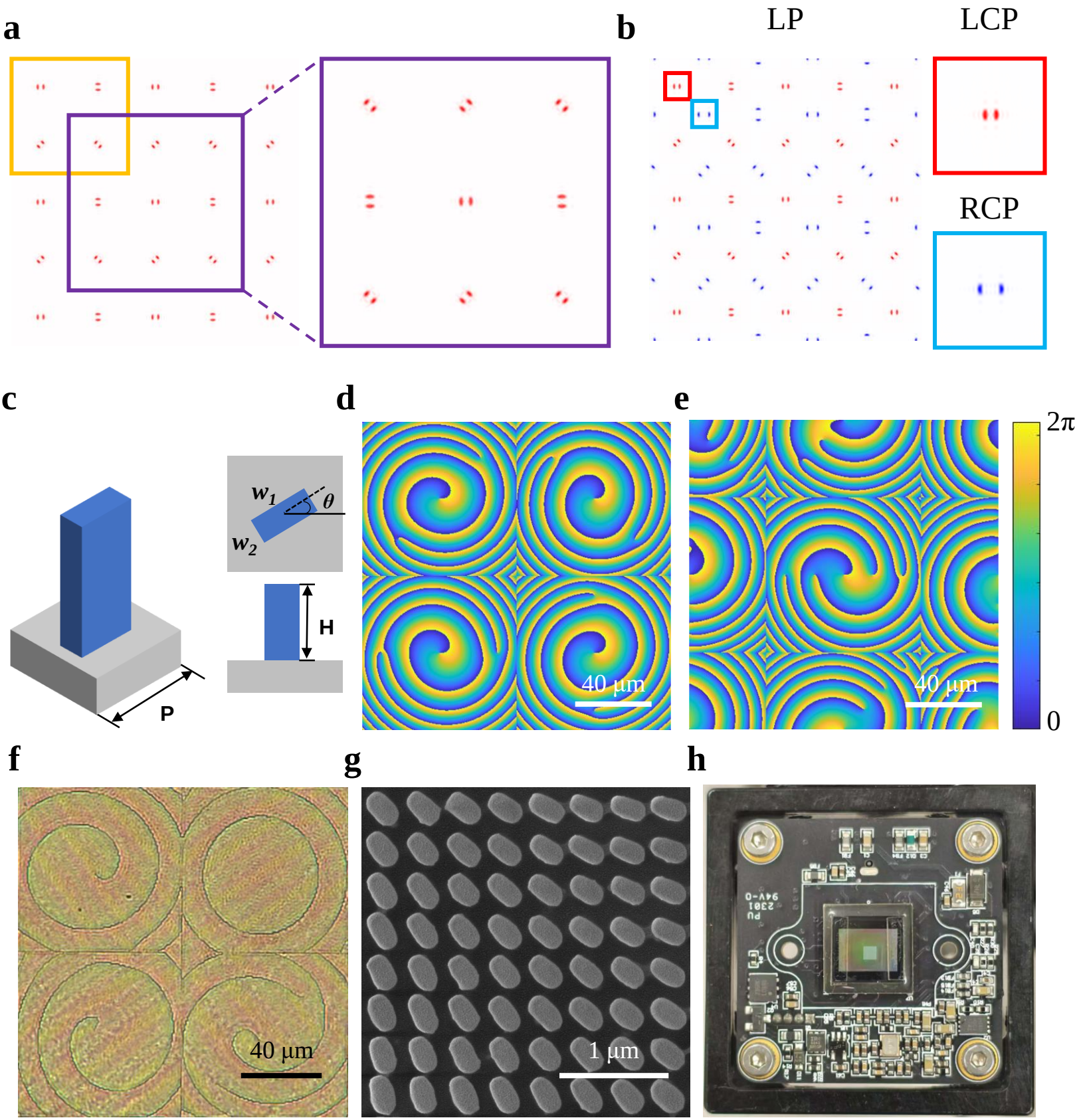
a
b
LP
LCP
RCP
c
w_1
w_2
θ
H
P
d
40 μm
e
40 μm
2π
0
f
40 μm
g
1 μm
h

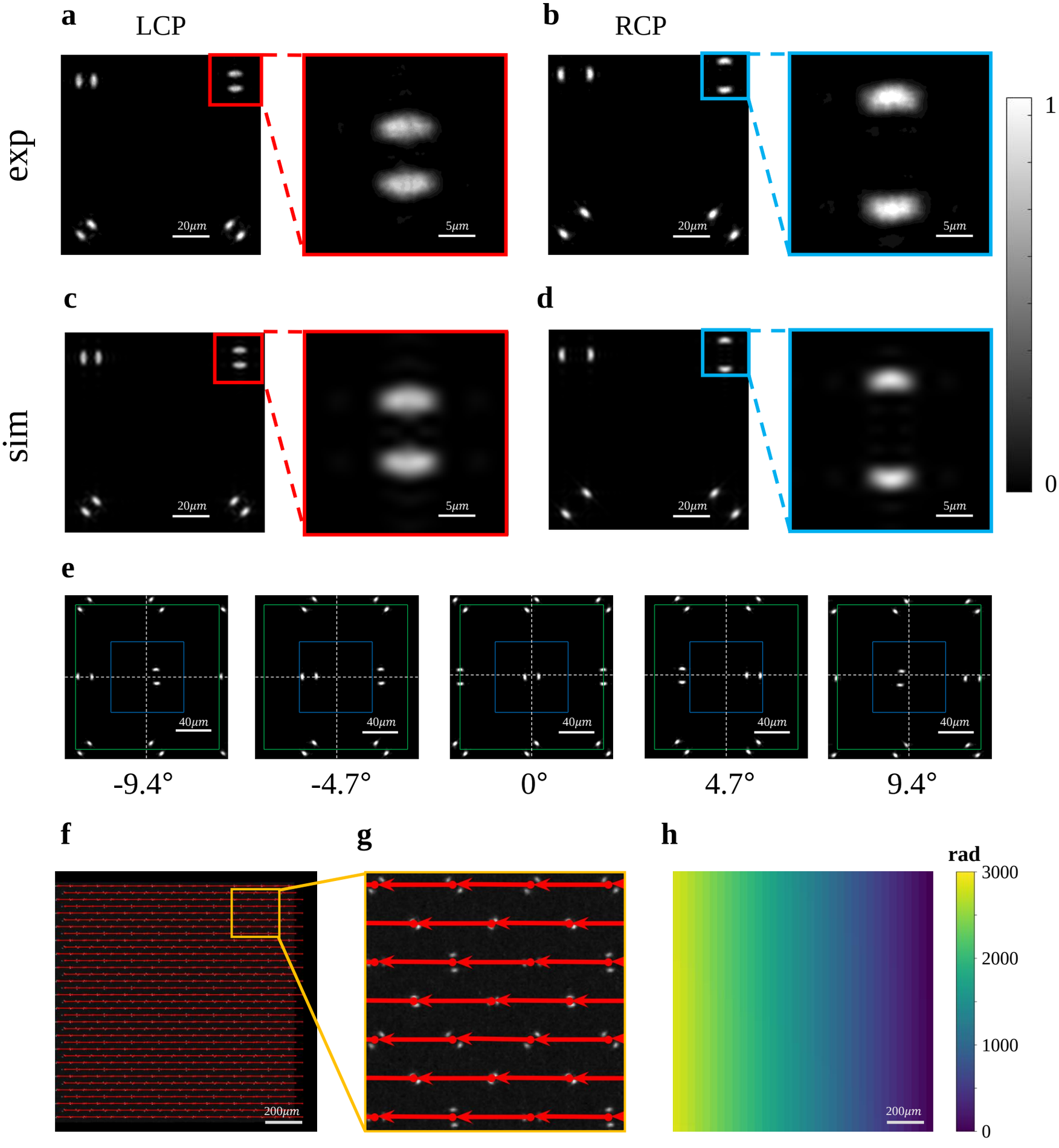
a
LCP
b
RCP
exp
20μm
5μm
20μm
5μm
1
0
c
d
sim
20μm
5μm
20μm
5μm
e
40μm
40μm
40μm
40μm
40μm
-9.4°
-4.7°
0°
4.7°
9.4°
f
g
h
rad
200μm
200μm
3000
2000
1000
0

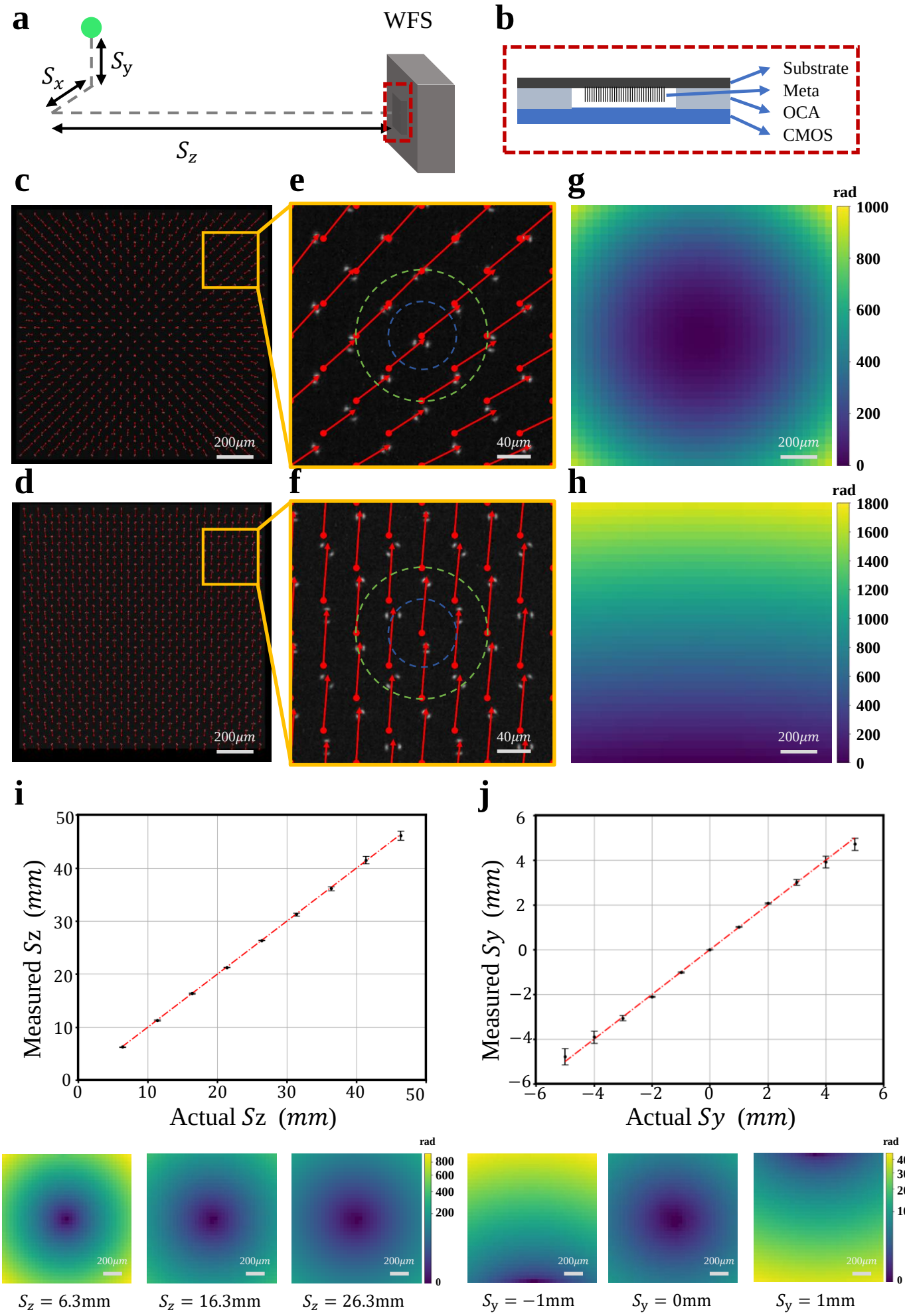
a
WFS
S_x
S_y
S_z
b
Substrate
Meta
OCA
CMOS
c
d
e
f
g
h
200μm
40μm
rad
1000
800
600
400
200
0
1800
1600
1400
1200
1000
800
600
400
200
0
i
Measured Sz (mm)
Actual Sz (mm)
j
Measured Sy (mm)
Actual Sy (mm)
S_z = 6.3mm
S_z = 16.3mm
S_z = 26.3mm
S_y = −1mm
S_y = 0mm
S_y = 1mm


a
b
Fitted Height
Ground Truth
Residual
μm
100
80
60
40
20
0
1
0
-1
200μm
c
Fitted Radius of Curvature
Nominal Radius of Curvature
Radius of Curvature (mm)
12
10
8
6
5.180
5.170
5.168
5.170
5.184
5.170
6.476
6.460
8.240
8.260
10.362
10.360
12.848
12.910
Sample 1
Sample 2
Sample 3
Sample 4
Sample 5
Sample 6
Sample 7

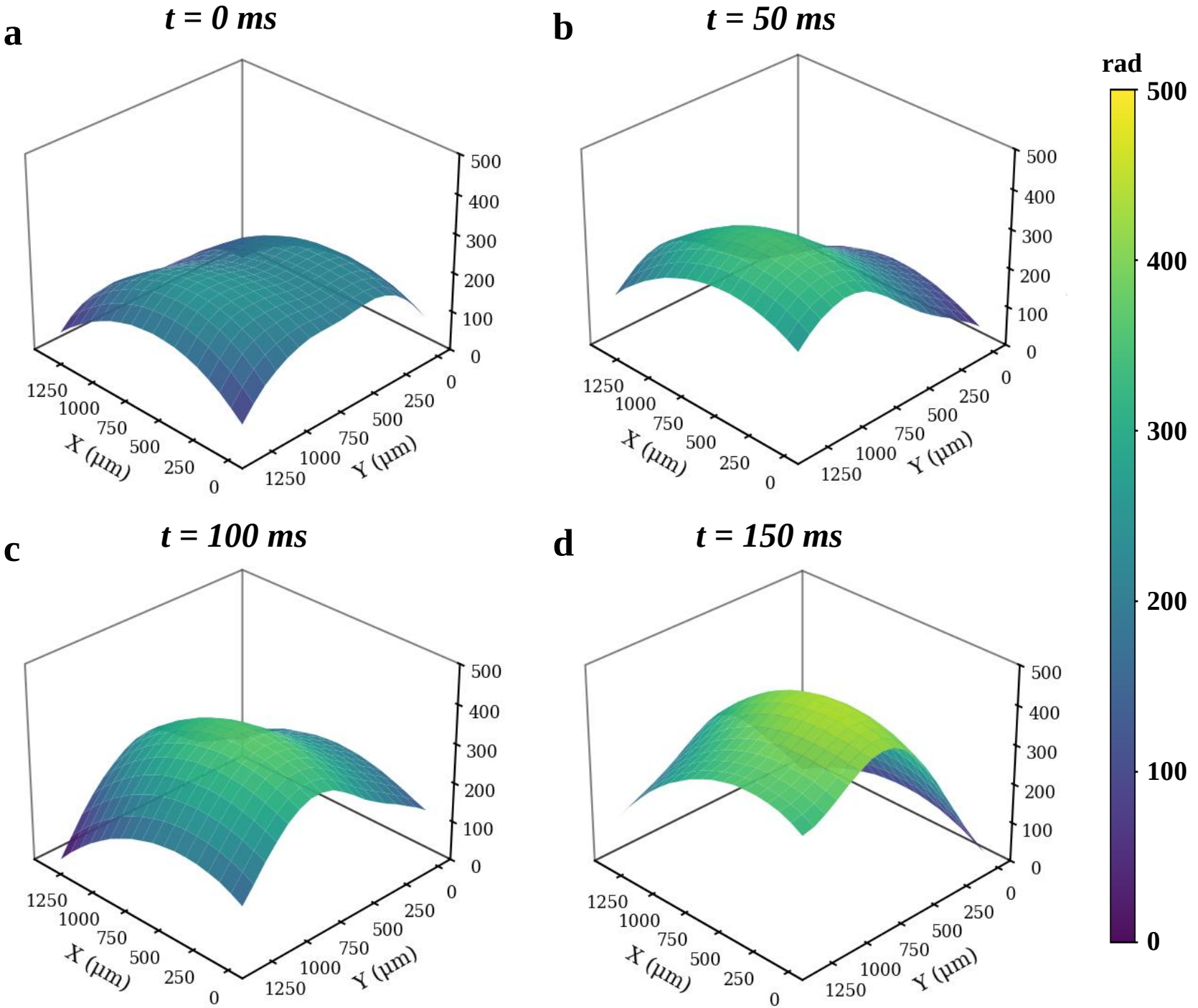
a
t = 0 ms
b
t = 50 ms
c
t = 100 ms
d
t = 150 ms
rad
500
400
300
200
100
0
X (µm)
Y (µm)
1250
1000
750
500
250
0

we present the first chip-integrated metasurface Shack-Hartmann sensor operating directly on a complementary metal oxide semiconductor image sensor without external optics. Our dual-encoding strategy uses orientation-encoded double-helix point spread functions to extend the dynamic range to $\pm 9.4°$ per channel without degrading sampling density, while orthogonal circular polarization channels with distinct lobe separations double the sampling density without sacrificing dynamic range. The architecture inherently supports vectorial wavefront sensing. We demonstrate three-dimensional localization of point source, lens profilometry, and video-rate dynamic wavefront monitoring, establishing a scalable platform for alignment-free, high-performance metrology.

Introduction

Wavefront sensing[1-4] is a cornerstone of modern optical systems, enabling critical capabilities in astronomical observations[5-6], free-space optical communication[7] to biomedical imaging[8-10]. As these fields increasingly demand compact, robust, and high-performance metrology tools, there is a growing need for wavefront sensors that combine ultra-large dynamic range, high spatial sampling density, compatibility with integrated photonic platforms, and sensitivity to vectorial (polarization-dependent) wavefront distortions.

Conventional Shack-Hartmann wavefront sensors (SHWFS)[11-12] have gained widespread adoption due to their straightforward design and operational simplicity. However, they are fundamentally constrained by the fabrication and physical limitations of refractive microlens

arrays[13]. The minimum pitch of conventional microlenses is typically around 100 μm, limiting the spatial sampling density to approximately 10 sub-apertures per millimeter[14]. To avoid ambiguity between adjacent spots under large wavefront tilts, the measurable tilt is restricted to half the microlens diameter, resulting in an intrinsic geometric dynamic range of only about ±1°, when considering the microlens array alone without algorithmic or hardware enhancements[15]. This geometric limit can be expressed as $\theta_{max} \approx \tan^{-1}(D/2f)$, where D is the microlens pitch and f is the focal length, corresponding to the maximum acceptance angle that can be unambiguously measured before a spot crosses into an adjacent sub-aperture's designated region. Moreover, conventional SHWFS lack any intrinsic capability to resolve polarization-dependent phase distortions, rendering them blind to vectorial wavefronts. Various hardware-based strategies, such as adjusting the relative positions of the microlens array and image sensor[16-18], integrating auxiliary sensing elements[19-21], employing tunable lenses[22-24], or utilizing nonlocal thin-film optical filters[25], along with algorithmic approaches like adaptive spot matching[26] and iterative fitting[27], have been explored to extend performance. Yet these methods often increase system complexity, reduce spatial resolution, or require intensive computation, and none fully resolve the core trade-offs.

Recently, metasurfaces[28-34] have recently emerged as a transformative platform for wavefront engineering, offering unprecedented control over phase, amplitude, and polarization at the subwavelength scale. Their compact form[35], compatibility with complementary metal oxide semiconductor (CMOS) processes, and potential for mass fabrication[36] make them highly promising for next-generation wavefront sensors. Several notable metasurface-based wavefront sensing schemes[7,37-38] have been demonstrated recently, showcasing the potential of this approach

for compact metrology. Nevertheless, all reported metasurface-based SHWFS[15, 39-42] to date still rely on external microscope objectives or relay optics to image the focal plane. This dependence compromises mechanical robustness, restricts the effective measurement aperture, and prevents true on-chip integration. Critically, despite their added degrees of freedom, existing metasurface implementations remain bound by the same inherent trade-off among dynamic range, spatial sampling density, and centroid localization accuracy that plagues conventional systems. There remains a lack of wavefront sensors that simultaneously achieve high integration, large dynamic range, high spatial sampling density, and polarization-resolved vectorial sensing.

In this work, we develop, for the first time, a chip-integrated metasurface SHWFS that operates directly on a CMOS image sensor without any external optics, overcoming the long-standing trade-off among dynamic range, spatial sampling density, and centroid localization accuracy. Our design employs a dual-encoding strategy based on double-helix point spread functions[43-47] (DH-PSF), which have been widely used in depth sensing and single-molecule localization. Here, we repurpose their characteristic lobe separation and orientation encoding to eliminate crosstalk under large wavefront tilts. Specifically, orientation-encoded DH-PSFs double the dynamic range per polarization channel without compromising sampling density, while orthogonal circular polarization channels with distinct lobe separations enable unambiguous interleaving of two sub-aperture arrays, doubling the sampling density without sacrificing dynamic range. The architecture inherently supports vectorial polarization wavefront sensing. Combined with single-shot operation and CMOS compatibility, this approach establishes a scalable, alignment-free paradigm for high-performance wavefront metrology across adaptive optics,

integrated photonics, and dynamic imaging applications.

Results

Design of metasurface wavefront sensor. The DH-PSF can be generated at the working wavelength of 532 nm by introducing vortex phase singularities in the pupil plane[46]. These vortex singularities are located roughly along a line through the center of a sub-aperture. In radial coordinates, the phase function of the metasurface for a single sub-aperture is given by:

$$\varphi(r,\theta) = \arg\left(\prod_{j=-M}^{M} \left(re^{i\theta} - r_j e^{i\theta_j} \right) \right) - \frac{kr^2}{2f}, \tag{1}$$

where (r, θ) are the pupil plane coordinates, (r_j, θ_j) is the location of the j-th vortex, arg denotes the argument (phase) of a complex number and $M=(N-1)/2$, N is the number of vortices, k is the wave vector and f is the focal length, r_j and θ_j are respectively defined as follows:

$$\begin{cases} r_j = |j| d \\ \theta_j = \dfrac{\pi}{2}\left(1 - \dfrac{j}{|j|}\right) + \theta_0, \; j \neq 0 \end{cases}, \tag{2}$$

where d is the distance between vortices, θ_0 denotes the orientation angle of the DH-PSF, defined as the angle between the line connecting its two main lobes and the x-axis. More detailed derivations are provided in Supplementary Note 1. The quadratic phase term in the function performs the Fourier transform. The main-lobe separations and efficiency of the resulting DH-PSF can be flexibly tuned by adjusting the inter-vortex separation d and the total number of vortices, N. By rotating the line of vortex singularities with respect to the x-axis, the orientation angle of the DH-PSF can be precisely tuned. Each vortex constitutes a phase singularity with a uniform charge

of +1, forcing the amplitude to zero at its center and thereby redistributing the energy into two lobes on opposite sides. This main-lobe separations and orientation angle provide additional, unambiguous features that can be used to differentiate individual PSFs, especially under conditions of large wavefront gradients.

To double the effective sampling density without compromising dynamic range, we employ the orthogonal circular polarization-multiplexed design to independently engineer the phase profiles for each polarization channel. This simultaneous control of left circular polarization (LCP) and right circular polarization (RCP) light is achieved within a single monolithic metasurface by combining propagation phase with Pancharatnam–Berry (PB) phase[48]. In one polarization channel, four sub-apertures form a basic periodic unit, as delineated by the orange square in Fig. 1(a), with the principal orientation angles of their DH-PSFs set to 0°, 90°, 45°, and 135°, respectively. This arrangement ensures that the PSF in each sub-aperture exhibits a distinct orientation relative to all its neighboring PSFs, as shown in the purple square in Fig. 1(a). Consequently, large wavefront gradients that induce substantial spot displacements no longer cause ambiguity between adjacent spots, due to the distinct encoding of each PSF. This allows spot shifts up to nearly the full sub-aperture diameter, which is double of the conventional limit of half the pitch, thereby doubling the dynamic range without crosstalk. The aperture distribution of the orthogonal polarization channel is interleaved with each other, as shown in Fig. 1(b), where red DH-PSFs denote the LCP channel and blue DH-PSFs denote the RCP channel. To prevent crosstalk between the two orthogonally polarized channels during simultaneous wavefront sampling, the main-lobe separation of the DH-PSFs is engineered as a discriminative dimension: the lobe spacing in the LCP channel (highlighted

by the red box in Fig. 1(b)) is set to one-half of that in the RCP channel (blue box in Fig. 1(b)). Under linearly polarized (LP) illumination, the wavefront is simultaneously sampled by the two orthogonal polarization channels as shown in Fig. 1(b). This design further breaks the traditional trade-off between sampling density and dynamic range in Shack-Hartmann sensors, enabling a doubling of the effective sampling density without compromising the measurement range.

The metasurface is composed of rectangular nanopillars with a height of 1 μm and widths w_1 and w_2, arranged in a periodical of 350 nm to satisfy the Nyquist criterion as shown in Fig. 1(c). The widths w_1 and w_2 are varied between 60 nm and 270 nm, enabling precise control over the local phase response. Silicon nitride is chosen as the structural material due to its low optical losses in the visible spectrum and compatibility with CMOS fabrication processes, facilitating scalable integration. Full wave electromagnetic simulations were performed using the commercial finite-difference time-domain (FDTD) solver (Lumerical FDTD) to model the optical response of the nanostructures (See Methods). Each sub-aperture is designed to operate at a wavelength of 532 nm, with a radius of 40 μm and a focal length of 470 μm to match the image plane of the CMOS sensor. The parameters *(d, M)* for the LCP and RCP channels are set to (30×10^{-6} m, 8), and (15×10^{-6} m, 10), respectively, ensuring that the generated DH-PSFs in both channels exhibit comparable main-lobe energy distributions while maintaining sufficiently distinct lobe separations. Detailed analysis of DH-PSF parameter selection is provided in Supplementary Note 1. Depicted in Fig. 1(d) and (e) are the phase profiles of a basic periodic unit for the LCP and RCP channels. A corresponding 100 × optical micrograph of the unit is provided in Fig. 1(f). The basic periodic unit is expanded into a 9×9 array, forming a wavefront sensor with 18×18 sub-apertures for the LCP channel and 17×

17 sub-apertures for the RCP channel (35×35 totally for LP channel). The overall dimensions of the sensor are 1.44 mm × 1.44 mm. The metasurface was fabricated through the preparation process detailed in Methods. Scanning electron microscope (SEM) images of the fabricated metasurface, shown in the Fig. 1(g), confirm high-fidelity patterning and periodic arrangement of the nanostructures. Finally, the fabricated metasurface is securely bonded onto the CMOS image sensor using an optically transparent adhesive (OCA8146-2, Thorlabs) as shown in Fig. 1(h). This adhesive serves not only as a mechanical binder but also as an optical coupling layer, enabling fine adjustment of the effective focal distance between the metalens and the imaging plane. A detailed discussion on its thermal and mechanical stability and its impact on reconstruction accuracy is provided in Supplementary Note 2. This alignment ensures sharp and well-resolved DH-PSFs are formed on the sensor surface.

Characterization of metasurface wavefront sensor. To validate the quality of the metasurface-generated DH-PSFs, we measured the intensity distributions from a basic periodic unit for both polarization channels, shown in Fig. 2(a) for LCP and Fig. 2(b) for RCP. The corresponding simulated intensity profiles, obtained via scalar diffraction calculation[49], are presented in Fig. 2(c) and Fig. (d), respectively. A direct comparison reveals excellent agreement between the experimental and simulated DH-PSFs in terms of both orientation angle and main-lobe separation. We further characterized the response of a single DH-PSF under collimated beam illumination at various incident angles. Figure. 2(e) displays the displacement trajectory of a representative DH-PSF in the RCP channel, measured under incident angles ranging from -9.4° to +9.4°. The blue rectangle indicates the maximum allowable displacement region for a conventional circular PSF,

whereas the green rectangle denotes the extended region achieved by our DH-PSF-encoded metasurface wavefront sensor. The results demonstrate that our approach doubles the dynamic range per polarization channel compared to circular PSFs, enabling unambiguous operation up to a $\pm 9.4°$ angular range without cross-talk.

Experimental validation confirms that our meta wavefront sensor achieves a dynamic range up to $\pm 9.4°$. This was tested by illuminating the integrated sensor with tilted plane waves, and the maximum recoverable angle was found to be $9.4°$, which is consistent with the maximum displacement limit of a single DH-PSF. The corresponding DH-PSF intensity pattern at the focal plane is shown in Fig. 2(f). Figure. 2(g) provides the zoom-in view of the orange-boxed region in Fig. 2(f), with the red arrow marking the PSF displacement vector relative to the normal-incidence reference. The successfully reconstructed wavefront corresponding to this tilt is presented in Fig. 2(h).

Complementing the upper bound of dynamic range, we also evaluated the sensor's sensitivity limit. The minimum resolvable angle θ_{min} is fundamentally limited by the pixel pitch of the CMOS sensor and the focal length of the metalens sub-apertures, yielding $\theta_{min} \approx 0.2°$ for our system. This corresponds to a minimum resolvable phase gradient of approximately 4.2×10^4 rad/m at the operating wavelength of 532 nm. A detailed derivation of this sensitivity limit is provided in Supplementary Note 3.

Three-dimensional localization of a point source. To validate the large dynamic range wavefront sensing, we demonstrate three-dimensional (3D) localization of a point source generated by focusing a beam through a $50\times$ microscope objective (NA=0.8). Figure. 3(a) illustrates the

schematic of the experimental setup. Figure. 3(b) shows a schematic layout of the WFS illustrated in Fig. 3(a). By scanning the point source along the optical axis (z) and the transverse direction (y), the sensor acquires wavefront information for 3D reconstruction. Figure. 3(c) and 3(d) show DH-PSFs intensity distributions in the focal plane at two representative positions during axial (z) and transverse (y) scanning of the point source, corresponding to the 3D coordinates (0, 0, 6.3 mm) and (0, 4.2 mm, 41.3 mm), respectively. The red arrows denote the displacement vector of the DH-PSF relative to its reference position under plane-wave illumination. Figure. 3(e) and Fig. 3(f) show the zoom-in views of the orange regions highlighted in Fig. 3(c) and Fig. 3(d), respectively. The blue circles denote the maximum allowable displacement region for a PSF initially centered within the circle under the conventional Shack-Hartmann sensing paradigm, whereas the green circles represent the extended displacement region enabled by our DH-PSF-encoded wavefront sensor design. This comparison visually demonstrates a two-fold enhancement in dynamic range over the traditional approach. Furthermore, the PSFs of the two polarization channels can be distinguished by their different main lobe spacings, thereby avoiding crosstalk. This design not only extends the dynamic range but also doubles the sampling density. By computing the relative displacements of the DH-PSFs, the local wavefront gradients are obtained, enabling reconstruction of the full wavefront, as shown in Fig. 3(g) and Fig. 3(h). Further details on the wavefront reconstruction algorithm are provided in the Supplementary Note 4, and a quantitative analysis of DH-PSF decoding robustness is presented in Supplementary Note 5. Figure. 3(i) and Fig. 3(j) show the high-precision localization results of the wavefront sensor for a point source scanned along the axial (z) and transverse (y) directions, respectively. Each subfigure illustrates the reconstructed

wavefronts at various sampling points.

Lens surface profilometry. The surface topography of transparent samples can be retrieved from the wavefront of transmitted light. Owing to high integration, the transmitted wavefront can be captured in a single snapshot simply by placing the sample directly above the sensor, enabling high-precision profilometry. As a proof-of-concept, we characterized plano-convex lenses with varying parameters. Figure. 4(a) show photographs of the experimental setup, where the sensor is mounted horizontally and the test lens is placed directly on its surface, with a collimated beam incident normally from above. As shown in Fig. 4(b), the relative height of a representative plano-convex lens was reconstructed (left), compared against the ground truth (middle), and their residual error was mapped (right). The minimal residuals observed attest to the high accuracy of the measurement. This high accuracy is further substantiated by testing lenses with different parameters. Figure. 4(c) compiles the results, where the fitted curvature radii (blue circles) consistently match the nominal values (red triangles), demonstrating the method's robustness across varied samples. Additional details can be found in the Supplementary Note 6. Our approach enables rapid, high-precision optical component inspection without complex alignment or reference arms.

Dynamic wavefront measurement at video frame rates. To validate dynamic sensing capability, a deionized water droplet was placed on the sensor surface and subjected to external vibration, inducing continuous deformation. The time-varying surface profile modulates the transmitted wavefront, generating an evolving phase distribution. The single-shot imaging architecture captures and reconstructs wavefront evolution at video frame rates. Figure. 5 presents the

reconstructed wavefronts at four representative time points, and the full dynamic reconstruction result is provided in Supplementary Movies 1. For further details on dynamic reconstruction capabilities, see Supplementary Note 7 and Supplementary Movies 2. This experiment demonstrates the dynamic wavefront sensing under non-stationary conditions. Our system enables scan-free, reference-arm-free, full-field tracking of instantaneous surface deformations at video rates, establishing a new paradigm for label-free dynamic surface metrology.

Discussion

We have proposed, for the first time, a chip-integrated metasurface SHWFS that overcomes the long-standing trade-off between dynamic range and spatial sampling density. Our dual-encoding strategy combines two synergistic mechanisms: first, orientation-encode DH-PSFs in each sub-aperture double the dynamic range per polarization channel to $\pm 9.4°$ by providing a unique angular signature that resolves spot ambiguity under large tilts without degrading sampling density; second, orthogonal circular polarization channels with distinct main-lobe separations enable unambiguous interleaving of two sub-aperture arrays, doubling the effective sampling density without sacrificing dynamic range. This decoupling of traditionally conflicting parameters represents a fundamental advance over both conventional and existing metasurface-based sensors, achieving, to the best of our knowledge, a record-breaking intrinsic geometric dynamic range ($\pm 9.4°$) in a chip-integrated SHWFS purely by hardware-level encoding, while room remains for further improvement through algorithmic enhancements and related approaches. The functional

advantage is validated by three experiments: (i) 3D point-source localization confirmed unambiguous gradient measurement within the extended range; (ii) surface profilometry of plano-convex lenses achieved high parameter accuracies; and (iii) continuous monitoring of an oscillating water droplet demonstrated its potential for dynamic profilometry of transparent interfaces.

Looking forward, our platform holds significant potential for further performance enhancement and functional expansion. While the current design is optimized for a single wavelength of 532 nm, by changing the material and redesigning the metasurface, this platform can be adapted to essentially any wavelength band. Moreover, future iterations could adopt achromatic metalens designs or depth-of-focus-optimized phase patterns to enable broadband operation, mitigating chromatic aberrations inherent to dispersive metasurfaces. The dynamic range per channel could be tripled, rather than merely doubled, by employing a finer angular encoding scheme for the DH-PSFs, though this would reduce the orientation tolerance from $\pm$ 22.5° to approximately $\pm 10°$. Furthermore, the inherent polarization multiplexing enables a powerful additional capability: polarization-resolved wavefront sensing. By independently processing the displacement information from the two channels, one can simultaneously decode the phase and polarization state of the incident light. This capability opens up prospects for future applications in scenarios involving polarization-resolved wavefront sensing. (see Supplementary Note 8). Regarding real-time operation, our computational analysis (Supplementary Note 9) confirms that the wavefront reconstruction step can achieve sub-millisecond latencies with optimized algorithms, and the highly parallelizable gradient measurement process is amenable to

hardware acceleration (e.g., Graphics Processing Units (GPUs) or Field-Programmable Gate Arrays (FPGAs)) for demanding adaptive optics applications requiring kHz-level loop rates.

In summary, by synergistically combining orientation encoding with polarization multiplexed main-lobe separations encoding DH-PSFs, our approach significantly enhances both dynamic range and sampling density while maintaining a compact, CMOS-compatible architecture—offering a practical and scalable solution for high-performance wavefront sensing.

Methods

Numerical simulations. The phase response of the nanopillars was obtained through numerical simulations based on the finite-difference time-domain (FDTD) method. The incident plane wave had a wavelength of 532 nm and circular polarization. The nanopillars were modeled on a fused silica substrate. Periodic boundary conditions were applied along the x- and y-axes, and perfectly matched layers (PMLs) were employed along the z-axis to absorb outgoing waves. The geometric parameters of the nanopillars are provided in the main text.

Device fabrication. The sample was fabricated using a standard process combining electron-beam lithography (EBL) and reactive ion etching (RIE). A 1-μm-thick silicon nitride (SiN_x) layer was first deposited onto a fused silica substrate via plasma-enhanced chemical vapor deposition (PECVD). A 200-nm-thick layer of PMMA A4 resist was then spin-coated onto the SiN_x surface and baked at 170 °C for 5 minutes. To mitigate charging effects during electron-beam exposure, a

42-nm-thick water-soluble conductive polymer (AR-PC 5092) was subsequently spin-coated on top of the resist. The device pattern was defined by electron-beam writing (Elionix ELS-F125) in the resist. After exposure, the conductive polymer was rinsed away with deionized water, and the resist was developed in an appropriate developer solution. A chromium hard mask was then formed through electron-beam evaporation followed by a lift-off process. This Cr mask was used to transfer the pattern into the underlying SiN_x layer via inductively coupled plasma reactive ion etching (ICP-RIE, Oxford Instruments PlasmaPro 100 Cobra 300), employing a gas mixture of CHF_3 and SF_6. Finally, the residual chromium was removed using a ceric ammonium nitrate-based stripping solution.

Data availability

The source data that support the findings of this study are provided in in the Figshare database at https://doi.org/10.6084/m9.figshare.32084904.

Code availability

The code that support the plots within this paper and other findings of this study are available from the corresponding author upon request.

References

1. Long, X. et al. In-Situ Wavefront Correction via Physics-Informed Neural Network. *Laser*

Photonics Rev. **18**, 2300833 (2024).

2. Yi, S. et al. Angle-based wavefront sensing enabled by the near fields of flat optics. *Nat. Commun.* **12**, 6002 (2021).
3. Li, W. et al. Single-pixel wavefront sensing via vectorial polarization modulation. Chin. *Opt. Lett.* **21**, 090008 (2023).
4. Hu, W. et al. High Spatial and Angular Resolution Wavefront Sensing Based on the Random Phase Modulated Diffraction Effect. *Laser Photonics Rev.* e00984 (2025).
5. Guo, Y. et al. Direct observation of atmospheric turbulence with a video-rate wide-field wavefront sensor. *Nat. Photon.* **18**, 935–943 (2024).
6. Liu, Q. et al. Research Progress on Atmospheric Turbulence Perception and Correction Based on Adaptive Optics and Deep Learning. *Adv. Photon. Res.* 2400204 (2025).
7. Martin Jimenez, A., Baltes, M., Cornelius, J., Aközbek, N. & Coppens, Z. J. Single-shot phase diversity wavefront sensing in deep turbulence via metasurface optics. *Nat. Photon.* (2025).
8. Kang, I. et al. Coordinate-based neural representations for computational adaptive optics in widefield microscopy. *Nat. Mach. Intell.* **6**, 714–725 (2024).
9. Ji, N. Adaptive optical fluorescence microscopy. *Nat. Methods* **14**, 374–380 (2017).
10. Wang, K. et al. Direct wavefront sensing for high-resolution in vivo imaging in scattering tissue. *Nat. Commun.* **6**, 7276 (2015).
11. Primot, J. Theoretical description of Shack–Hartmann wave-front sensor. *Opt. Commun.* **222**, 81–92 (2003).
12. Fan, R. et al. Metasurfaces in Adaptive Optics: A New Opportunity in Optical Wavefront

Sensing. *Laser Photonics Rev.* e01566 (2025).

13. Akondi, V. & Dubra, A. Shack-Hartmann wavefront sensor optical dynamic range. *Opt. Express* **29**, 8417 (2021).
14. Soldevila, F. et al. Phase imaging by spatial wavefront sampling. *Optica* **5**, 164 (2018).
15. Go, G.-H. et al. Meta Shack–Hartmann wavefront sensor with large sampling density and large angular field of view: phase imaging of complex objects. *Light Sci. Appl.* **13**, 187 (2024).
16. Molebny, V. V. Scanning Shack-Hartmann wavefront sensor. in (ed. Kamerman, G. W.) 66 (Orlando, FL, 2004).
17. Lee, W. W. et al. Increase of dynamic range of a Shack-Hartmann sensor by shifting detector plane. in (eds. Jiang, W. & Suzuki, Y.) 70 (Beijing, China, 2004).
18. Xu, H. et al. Extended-aperture Hartmann wavefront sensor with raster scanning. *Opt. Express* **29**, 34229 (2021).
19. Lindlein, N. Expansion of the dynamic range of a Shack-Hartmann sensor by using astigmatic microlenses. *Opt. Eng.* **39**, 2220 (2000).
20. Lindlein, N. Experimental results for expanding the dynamic range of a Shack-Hartmann sensor using astigmatic microlenses. *Opt. Eng.* **41**, 529 (2002).
21. Saita, Y. et al. Holographic Shack–Hartmann wavefront sensor based on the correlation peak displacement detection method for wavefront sensing with large dynamic range. *Optica* **2**, 411 (2015).
22. Choo, H. et al. Addressable Microlens Array to Improve Dynamic Range of Shack–Hartmann Sensors. *J. Microelectromech. Syst.* **15**, 1555–1567 (2006).

23. Hongbin, Y. et al. A tunable Shack–Hartmann wavefront sensor based on a liquid-filled microlens array. *J. Micromech. Microeng.* **18**, 105017 (2008).

24. Martínez-Cuenca, R. et al. Reconfigurable Shack–Hartmann sensor without moving elements. *Opt. Lett.* **35**, 1338 (2010).

25. Li, L. et al. Single-Shot Wavefront Sensing with Nonlocal Thin Film Optical Filters. *Laser Photonics Rev.* **17**, 2300426 (2023).

26. Yang, J. et al. Large dynamic range Shack-Hartmann wavefront sensor based on adaptive spot matching. *Light: Advanced Manufacturing* **4**, 7(2024).

27. Groening, S. et al. Wave-front reconstruction with a Shack–Hartmann sensor with an iterative spline fitting method. *Appl. Opt.* **39**, 561 (2000).

28. Li, T. et al. Revolutionary meta-imaging: from superlens to metalens. *Photonics Insights* **2**, R01 (2023).

29. Li, L. et al. Metalens-array–based high-dimensional and multiphoton quantum source. *Science* **368**, 1487–1490 (2020).

30. Wang, S. et al. A broadband achromatic metalens in the visible. *Nat. Nanotechnol.* **13**, 227–232 (2018).

31. Chu, Y. et al. Achromatic multi-level diffractive lenses and related applications. *Advances in Physics: X* **10**, 2580626 (2025).

32. Khalid, A. U. R. et al. Single-layered non-interleaved spin-insensitive metasurfaces for wavefront engineering. *Chin. Opt. Lett.* **21**, 010006 (2023).

33. Chu, Y. et al. Design of achromatic hybrid metalens with secondary spectrum correction. *Opt.*

Express **31**, 21399 (2023).

34. Chu, Y. et al. Full-space wavefront control enabled by a bilayer metasurface sandwiching 1D photonic crystal. *Opt. Lett.* **48**, 5895 (2023).
35. Ye, X. et al. Chip-scale metalens microscope for wide-field and depth-of-field imaging. *Adv. Photon.* **4**, (2022).
36. Choi, M. et al. Roll-to-plate printable RGB achromatic metalens for wide-field-of-view holographic near-eye displays. *Nat. Mater.* **24**, 535–543 (2025).
37. Li, L. et al. Single-shot deterministic complex amplitude imaging with a single-layer metalens. *Sci. Adv.* **10**, eadl0501 (2024).
38. Li, L. et al. Monocular complex amplitude imaging via a polarization-multiplexed liquid-crystal-lens-informed Fourier neural network. *Natl Sci. Rev.* nwaf561 (2025).
39. Hu, Y. et al. Pitch-Switchable Metalens Array for Wavefront Profiling at Multiwavelength. *Adv. Opt. Mater.* **12**, 2302934 (2024).
40. Li, L. et al. Dielectric Metalens Array for Simultaneous Polarization and Wavefront Mapping in the Visible Spectrum. *Nano Lett.* **25**, 10879–10887 (2025).
41. Wang, Y. et al. Dielectric metalens-based Hartmann–Shack array for a high-efficiency optical multiparameter detection system. *Photon. Res*. **8**, 482 (2020).
42. Yang, Z. et al. Generalized Hartmann-Shack array of dielectric metalens sub-arrays for polarimetric beam profiling. *Nat. Commun.* **9**, 4607 (2018).
43. Shen, Z. et al. Monocular metasurface camera for passive single-shot 4D imaging. *Nat. Commun.* **14**, 1035 (2023).

44. Jin, C. et al. Dielectric metasurfaces for distance measurements and three-dimensional imaging. *Adv. Photon.* **1**, 036001 (2019).

45. R. Berlich, et al. Single shot three-dimensional imaging using an engineered point spread function. *Opt. Express* **24**, 5946 (2016).

46. Grover, G. et al. Super-resolution photon-efficient imaging by nanometric double-helix point spread function localization of emitters (SPINDLE). *Opt. Express* **20**, 26681 (2012).

47. Pavani, S. R. P. et al. High-efficiency rotating point spread functions. *Opt. Express* **16**, 3484 (2008).

48. Xu, B. et al. Metalens-integrated compact imaging devices for wide-field microscopy. *Adv. Photon*. **2**, (2020).

49. Goodman, J. W. Introduction to Fourier Optics (McGraw-Hill, New York, 1968).

Acknowledgements

The authors acknowledge the micro-fabrication center of the National Laboratory of Solid State Microstructures (NLSSM) for technique support.

Funding

T.L. discloses support for the research of this work from the National Key Research and Development Program of China (No. 2022YFA1404301), the National Natural Science Foundation of China (Grant No. 62325504), and the Fundamental Research Funds for the Central Universities (Grant No. KG202513). S.N.Z. discloses support for the research of this work from the National Natural Science Foundation of China (Grant No. 62288101). X.L. discloses support

from the Postdoctoral Fellowship Program of China Postdoctoral Science Foundation (Grant No. GZC20250558). Y.H.C., X.P.L., J.C.S., J.L., J.T.J., and J.Y.W. declare no relevant funding.

Author Contributions

Y.H.C., X.L., and T.L. conceived the idea; Y.H.C. designed and simulated the metasurface. X.P.L. developed the phase retrieval algorithm; X.L. and Y.H.C. designed the experiments; J.C.S. and J.L. fabricated the samples; Y.H.C., X.P.L., and X.L. performed the experiments; J.C.S. and J.T.J. acquired the scanning electron microscopy (SEM) images. Y.H.C., X.P.L., X.L., J.Y.W., S.N.Z. and T.L. analyzed the results; Y.H.C., X.P.L. drafted the manuscript with the help of X.L. and T.L.; T.L. supervised the entire project.

Competing interests

The authors declare no conflicts of interest.

Fig.1 Design of meta wavefront sensor. a Arrangement of DH-PSFs in the sub-apertures of the LCP channel. The orange square indicates a periodic unit of four sub-apertures (DH-PSF orientations: 0°, 90°, 45°, 135°). The purple square shows each PSF has a unique orientation relative to neighbours. **b** Interleaved layout of DH-PSFs in the orthogonal dual-polarization channels. Red and blue boxes highlight the two channels, with lobe spacing in the red box half that in the blue box to avoid crosstalk. LP: linear polarization, LCP: left circular polarization, RCP: right circular polarization. **c** Schematic of the metasurface unit cell structure. **d** Phase profiles of a basic periodic unit for the LCP channels. **e** Phase profiles of a basic periodic unit for the RCP channels. **f** 100× optical microscope image of a basic periodic unit. **g** Scanning electron microscope (SEM) images of the fabricated SiNx metasurface. **h** Photograph of chip-integrated metasurface wavefront sensor.

Fig.2 Experimental characterization of meta wavefront sensor. a–**b** Measured DH-PSF arrays in the LCP and RCP channels, showing periodic orientation patterns (0°, 90°, 45°, 135°), with representative 90°-oriented DH-PSFs highlighted by red and blue boxes, respectively. **c**–**d** Corresponding simulation results, showing excellent agreement with experiments. **e** Behaviors of a single PSF for different angles of incidence. Blue rectangles indicate the maximum allowable displacement region for a conventional circular PSF, the green rectangle denotes the extended region achieved by our design. **f** Measured intensity

distributions of the DH-PSFs in the focal plane. **g** Magnified views of the orange regions highlighted in **f**. **h** Reconstructed tilt wavefronts. LCP: left circular polarization, RCP: right circular polarization, exp: experiment, sim: simulation.

Fig.3 Three-dimensional (3D) localization of a point source. a Schematic of the experimental setup. **b** Cross-sectional illustration of the sensor structure. **c-d** Measured intensity distributions of the DH-PSFs in the focal plane. **e-f** Magnified views of the orange regions highlighted in (c) and (d), respectively. **g-h** Reconstructed wavefronts from the DH-PSF displacements. **i-j** Comparison between the measured and actual positions of the point source along the axial (z) and transverse (y) directions. Error bars represent standard deviation (SD) from independent measurements. Subfigures show wavefronts reconstructed at different positions. WFS: wavefront sensor, Meta: metesurface, OCA: optical coupling adhesive, CMOS: complementary metal oxide semiconductor.

Fig.4 Lens surface profilometry. a Photograph of the experimental setup, with the lower oblique view image showing a magnified region (red box) from the upper side view. **b** Fitted height distribution of the lens surface relative to its vertex (left), Ground Truth (middle) and Residual (right) between Fitted height and Ground Truth. **c** Comparison between the actual and reconstructed radii of curvature for lenses with different parameters. Blue circles: fitted radius of curvature; red triangles: nominal radius of curvature.

Fig. 5 Dynamic wavefront measurement at video frame rates. a-d Measured wavefront distributions at four representative time points.

Editorial summary:
A chip-integrated metasurface wavefront sensor operating without external optics uses orientation and lobe-spacing encoding of double-helix point spread functions, enabling a ±9.4° dynamic range and doubled sampling.

Peer review information: *Nature Communications* thanks Yuanmu Yang, Jangwoon Sung and Meiyan Pan for their contribution to the peer review of this work. A peer review file is available.